# 4 Detector components and integration

Corrado (5) DRAFT V1

This chapter ....

## 4.1 Requirements and challenges

The mechanics and cooling must accomplish the following requirements.

- **Layout:** Beam pipe, reduced outer radius 16.5 mm, 0.5mm wall thickness. Outside boundary condition not considered
- **Coverage:** Vertex detector constituted by 3 layers at coverage of the radii = 18-24-30 mm and $\eta$ coverage $\pm 2.5$ - $\pm 2.3$ - $\pm 2$ .
- **Hermeticity:** Equatorial gap between (active area of) matching a half-barrel: 1 mm
- **Mechanical gap:** avoid half-layer contact between matching half-barrel and avoid contact between L0 and beampipe (1.5mm nominal on the radius)
- **Alignment tolerance:** tolerance on the position of large-area sensors in space $< \pm 500 \mu$m
- **Access:** detector installation and services are only on A-side of the ALICE experiment.
- **Installation:** The installation concept will follow the same as ITS2. The new Detector barrel will interface with a service barrel same or equivalent to the existing one.
- **Fast insertion/removal for yearly maintenance:** Possibility to replace half barrels during YETS ($\sim$3 months)
- **Cooling:** Sensor operative temperature $<40^{\circ}$C , Sensor maximum temperature non-uniformity $<10^{\circ}$C
- **Material budget:** Material/layer: 0.05%$X_0$ average, minimise material in the sensitive region;
- **Sensor stability:** short-term (cannot be calibrated) $\leq$ detector position resolution $\sim 5$ $\mu$m, ensure high accuracy in the relative position of the detector sensors;
- **Radiation hardness:** TID radiation hardness <10 KGy, NIEL radiation hardness 1.x$10^{13}$ 1MeV $n_{eq}/cm^2$
- **Flammability:** Comply with LHC Fire Safety Instruction (IS-41)

The previous requirements push the mechanics and cooling design to face new challenges for vertex detectors:

- Integrate the smallest and thinnest beam pipe section never installed before in an LHC experiment.
- keep the large-area sensors safely bent and in perfect cylindrical shape while guaranteeing their proper working over the entire detector lifetime.
- Place the first layer (L0) at 1 mm of the beam pipe wall while guaranteeing the closure of the two half detectors with a gap of 1 mm.

## 4.2 Detector layer

The basic building block of the ITS3 is the detector layer. There is a total of three different layers with radii of 18, 24 and 30mm. Each layer (L0, L1, L2) is divided into two half-layers (H-L0, H-L1, H-L2). The conceptual design adopted for all the half-layers is illustrated in Figure 4.1 and it is based on the following elements:

- **Large-area silicon sensor (or silicon h-layer):** One single thin bent sensor covers an entire half- cylindrical layer. In line with the specifications, the sensor's pixel active area extends over a longitudinal length of approximately 260 mm and the sensor electrical interconnection is foreseen on the A-side.
- **Flexible printed circuits (FPCs):** A polyimide flexible printed circuit provides the data and powering transmission at the A-side, while an additional FPC provide powering transmission to the sensor at the C-Side. The electrical interconnection between the h-layer and FPC is through wire bonding (baseline).
- **Lightweight support structures:** Two longerons are placed at the long edges of the silicon sensor and provide mechanical support along the z direction; while two Half-Rings are placed at the bent extremity edges of the sensor. An additional H-Ring is placed at the extremity of the FPC facing the silicon H-Layer. It keeps the FPC bent and correctly aligned with the silicon H-Layer.
- **Radiator half-ring:** The H-Ring at the A-side also acts as a thermal radiator.
- **Gas distributor:** These structures correctly distribute and control the gas flow at the A-side and C-side.
- **Patch Panel 1 (PP1):** It provides support for the two FPCs, A-side and C-side, housing for the FPc electrical connectors and gas distributor fittings. The A 3D printed polymer

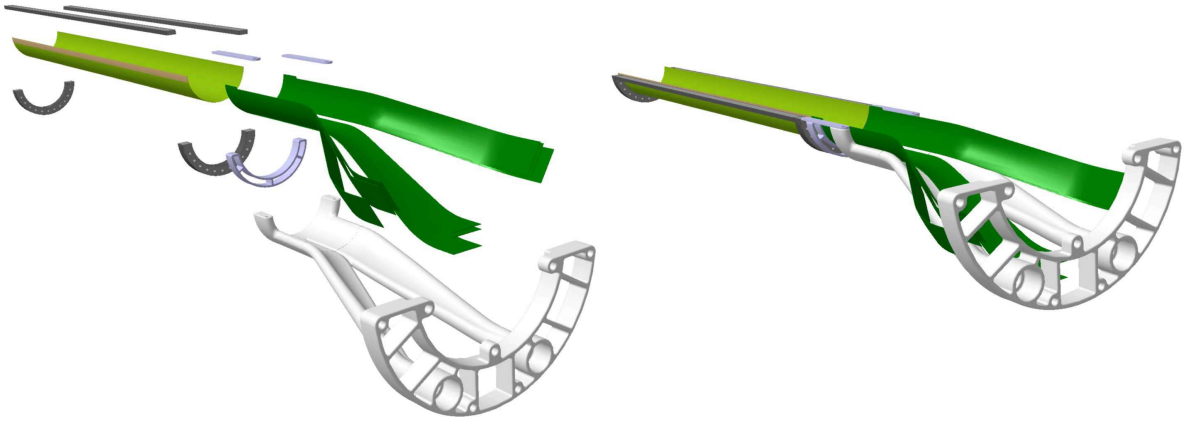

**Figure 4.1:** Schematic view of the half-layer 0. (a) Exploded view and (b) assembled view.

### 4.2.1 Material budget

WT Silicon to be discussed, plot to be discussed The design of the half layer accounts for the tight requirement on the material budget, whose target is 0.05 % $X_0$ for the first layer. Table 4.1 and Figure 4.2 report the estimated contributions of each half-layer element to the material budget. Plot of L0 material budget

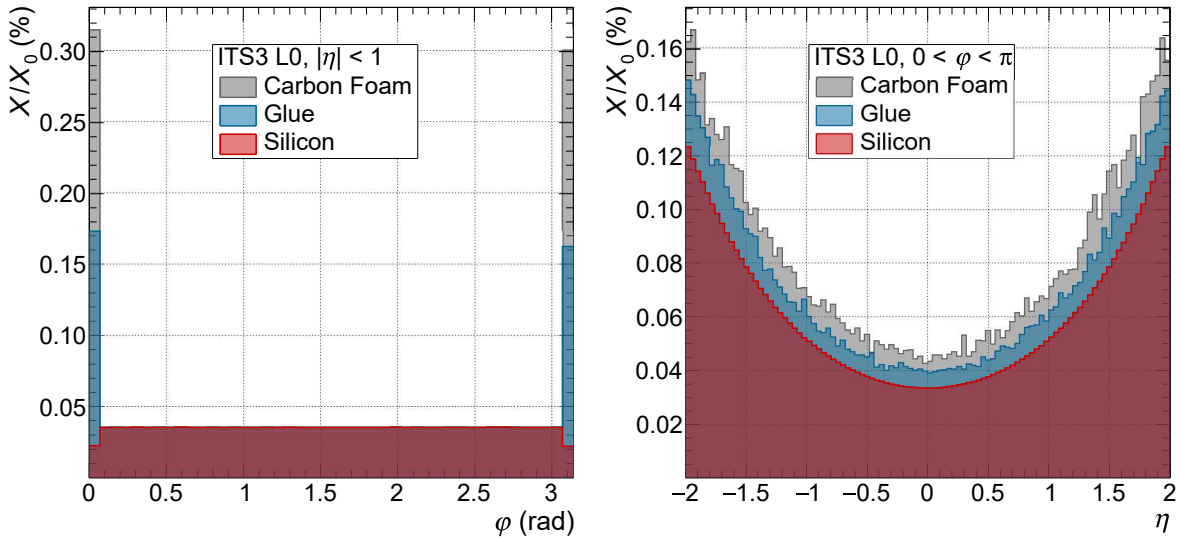


**(a)** $X/X_0$ Vs $\varphi$ ($Z_{vtx} = 0$) **(b)** $X/X_0$ Vs $\eta$ ($Z_{vtx} = 0$)

**Figure 4.2:** Material budget evaluation for L0. new pictures from Fabrizio, Andrea..

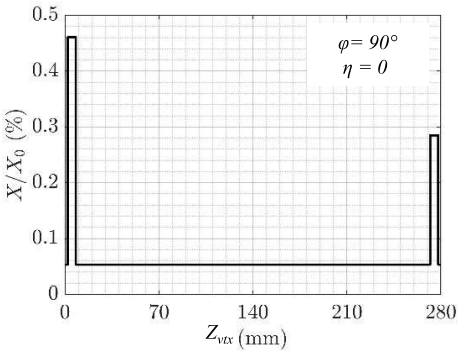


**Figure 4.3:** Material budget evaluation for L0. new pictures from Fabrizio, Andrea. .

**Table 4.1:** Estimated contributions of the material budget in layer 0. to be done

| Element | Material | | Density | $X_0$ [cm] | WT [mm] | $X/X_0$ [%] |
|---|---|---|---|---|---|---|
| Si sensor | Silicon | | | 9.369 | 0.03 | 0.032 |
| Mechanical support | Carbon foam | RVC | | 708.277 | 5.6 | 0.08 |
| | Glue + Fleece | Araldite 2011+ Carbon Fiber | | 58.62 | 0.4 | 0.07 |
| Radiator | Carbon foam | | | | | |
| | Glue | | | | | |

## 4.3 Mechanics and cooling

### 4.3.1 Design

The vertex detector is divided into two halves, top and bottom *"H-detectors"*, which are mounted separately around the beam pipe. Each H-Detector ( Figure 4.4) is composed of three "*H-layers*" (H-L0, H-L1, H-L2). Based on the low material budget requirement, on the H-Layer fragility and on the non-negligible forces required to keep them bent and in the correct position the H-layers are jointly glued one inside the next with the outermost, HL-2, bonded to an external Cylindrical Structural Shell (CYSS), that provide the main mechanical support. In this way, the force required to hold each layer is transferred between the H-Layer structural supports, which are under a compression stress regime, to the CYSS. This concept makes the H-detector the minimum replaceable component.

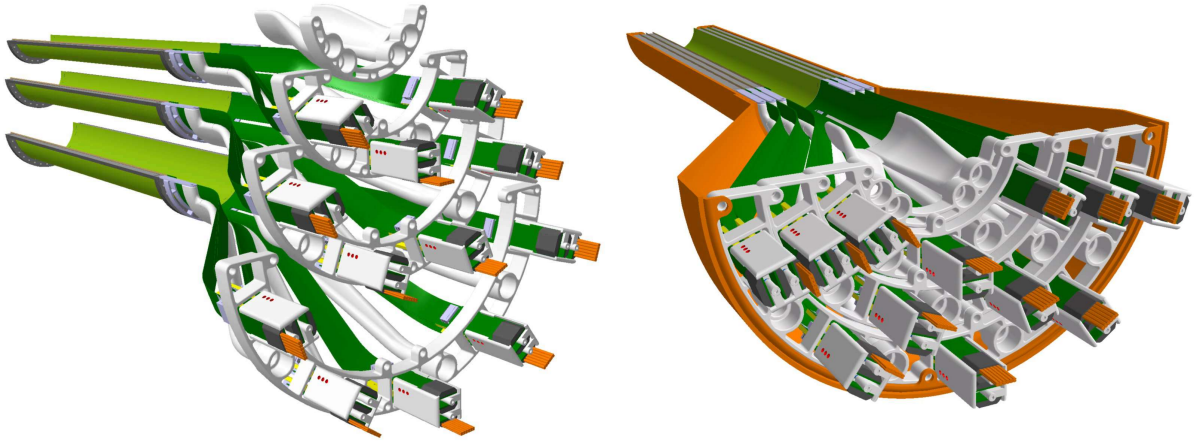

**Figure 4.4:** Half-detector.

Taking into account the total dissipated heat, air cooling is chosen to remove the heat dissipated by the sensor and to cope with the requirement of a maximum temperature difference in the overall detector of 10 degrees. Due to the concentration of power dissipation at the sensor end-cap on the A-side, carbon foam rings matching the high power dissipation region, act as a radiator by enhancing the heat exchange with the airflow. Carbon (graphite) foam with high thermal conductivity has been chosen for the rings on the A-side that act as radiator, while additional rings on the C side and longerons that run along the layers' edges are in carbon foam with lower density and slightly worst thermal properties. The carbon foam has been chosen for both thermal and structural part due to the extermely low material budget versus volume fraction.

Preliminary CFD simulations have shown that a single air flow distribution channel for the entire H-Barrel does not allow the control of the temperature distribution in the single layers. For this reason the design of the air distribution system foresees four separated channels, cooling the volumes in between layers, CYSS and beampipe.

### 4.3.2 Materials and production processes

The materials choice for the structural and thermal design has been driven by the unprecedented requirement on minimum material budget and stability over time.

### Carbon foam

Carbon foam has been identified as the material most suitable to fulfill the different requirements also based on the possibility to find on the market different variant of this material that cover a wide range of mechanical and thermal properties. Depending on the purpose of the component, structural support or radiator, two different types of open-cell carbon foams have been selected:

- **Structural support:** Reticulated Vitreous Carbon (RVC) Duocel®. One of morphological structures of the vitreous carbon manufactured by ERG Aerospace. This foam is a thermal insulator (see Table 4.2), although its low density and high Young modulus $E$ motivate its use as a structural part. The cell structure is isotropic, consisting of multiple cells of microscopic characteristic size (see Fig. 4.5a).
- **Radiator:** Allcomp K9 standard density. This foam manufactured by Lockheed Martin is made of RVC as a base material, with graphite added by chemical vapor deposition to increase its thermal conductivity $\kappa_f$ (see Table 4.2). The porosity $\Phi$ is still low despite the addition of the graphite. The microscopic structure is the same as the one of the RVC, with smaller cell sizes $\ell_{cell}$ (see Fig. 4.5b), which leads to a high specific surface area $\Sigma_s$. This is beneficial for the conductive heat transfer, since the heat transfer rate is proportional to this parameter.

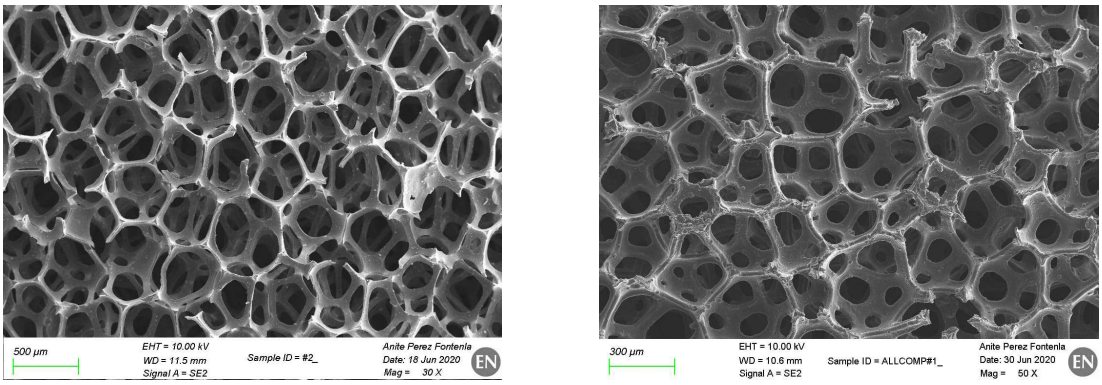


**(a)** RVC **(b)** K9

**Figure 4.5:** Microscopy images of the carbon foams used in the ALICE ITS3 cooling system

| Foam | $\rho$ (kg/m$^3$) | $\Phi$ | $\ell_{cell}$ ($\mu$m) | $\Sigma_s$ (1/m) | $\kappa_f$ (W/(m·K)) | $E$ (GPa) |
|---|---|---|---|---|---|---|
| RVC | 45 | 0.97 | 390 | 6600 | 0.05 | 0.1 |
| K9 | 200 | 0.89 | 285 | 14700 | 25 | 0.4 |

**Table 4.2:** Approximate parameters of the foams to be used in the ALICE ITS3 cooling system

The foams, when air flow through, produce a pressure loss that needs to be known to assess their performance, and an experimental setup has been built at CERN for this purpose (see Fig. 4.6). The geometry of the foams tested are rectangular cubes of $\ell_x \times \ell_y \times \ell_z = 6 \times 60 \times 6$ mm that represent characteristic dimensions of the foams to be used in the ALICE ITS3.

In addition to the experiments, computational model of the microscopic model of foams has been developed. This model considers a 14-sided truncated octahedron as a unit cell for the foams. The dimensions of the unit cell for each foam are completely determined by specifying the values of the porosity and the specific surface area, which are known parameters (see Table 4.2). By considering periodic boundary conditions for the unit cell, the pressure loss is obtained numerically from Computational Fluid Dynamics (CFD) simulations.

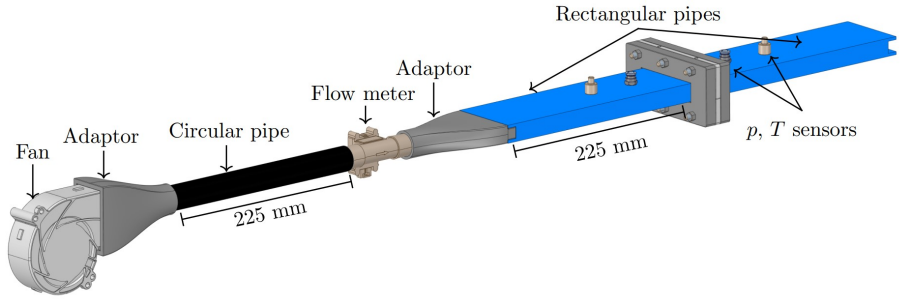


**Figure 4.6:** Experimental setup for the measurement of the foam pressure loss

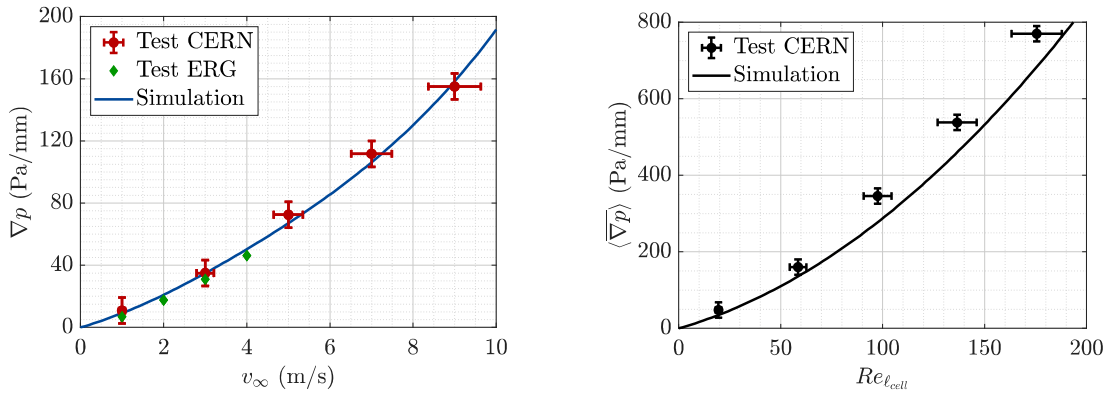


**(a)** Duocel® RVC **(b)** K9

**Figure 4.7:** Comparison between results of the simulations and experimental data of the pressure loss produced by the structural and the radiator foams

Experiments performed at CERN in the setup illustrated in Fig. 4.6 and data provided in the official website of ERG Aerospace are taken as a reference for result comparison. Fig. 4.7 compares the numerical results given by the macroscopic model and from experimental data. It is shown that the results of the tests and the simulations agree notably at all values of the freestream velocity $v_\infty$ for the Duocel® and K9 foams.

The computational model is also used to predict the thermal conductivity of the K9 foam, which is compared to data provided by the manufacturer of the foam. Fig. 4.8a illustrates the experimental results obtained from the laser flash method (Test A), from the direct contact method (Test B), and from the simulations of the K9 foam. The scattering of the experimental data is due to the lack of repeatability of the production process. A test performed at CERN for $\Phi = 0.89$ has given a value $\kappa_f = 25\ \mathrm{W\,m^{-1}\,K^{-1}}$, which is approximately the same as the mean values of the experimental data and the numerical value. This is the reference value used for subsequent simulations. The heat transfer coefficient has been calculated with the computational model (see Fig. 4.8b). These values are also used in the simulations of the ITS3 cooling system.

### Glues

A review has been done about the thermally-conductive glues (epoxy+filler). The glues used in other experiments at CERN have been studied, and alternatives have been searched on the market. The candidates for testing have been chosen in terms of the following properties:

- Viscosity: It should be low enough so that the glue penetrates into the foam, but not too low, because in that case the material budget increases. From previous detectors, a reference in terms of viscosity is the Araldite 2011 with $\mu = 40$ Pa s.

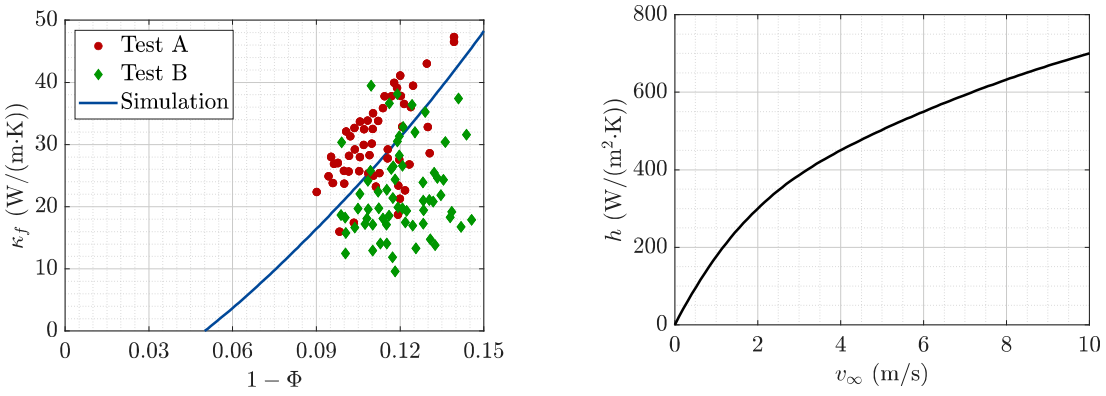


**(a)** Thermal conductivity **(b)** Heat transfer coefficient

**Figure 4.8:** Additional properties of the K9 foam

- Thermal conductivity: It should be as high as possible.
- Radiation length: Fillers are limited to graphite, boron nitride, and alumina for material budget reasons.
- Particle size: It should be as low as possible to reduce the damage to the silicon sensors.
- Electrical conductivity: The adhesive should be an electrical insulator to contribute to the grounding and shielding tasks.
- Young modulus and ultimate shear strength: The foam must keep the sensors into cylindrical shape. Thus, thermal gels are not taken into account.
- Coefficient of thermal expansion (CTE): It should be as close as possible to the one corresponding to silicon ($\approx 2.5 \times 10^{-6}$ K$^{-1}$) and carbon ($\approx 10^{-6}$ K$^{-1}$).
- Curing temperature: Curing at higher temperatures than room temperature induces thermal stresses. Thus, the glues considered are the ones that can be cured at temperature.
- Water absorption and flammability: Water absorption should be minimized to avoid the degradation of the thermal interface, and the adhesive should meet the standard for safety of flammability UL94-V0.

Based on the previous requirements, three glues have been purchased to test them in a thermal conductivity setup built at CERN by the EP-DT department (see Table 4.3). The Polytec TC 423-2 (P-423-2) has not been tested because the pot-life of the glue is extremely low after the parts are mixed. Three different samples have been tested of each glue to study the repeatability of the process. After verifying the accuracy of the setup first with the Araldite 2011, the results show great repeatability in the thermally-conductive glues. Given the importance of the thermal stresses due to the fragility of the structure, the Epoxies® 50-3150 FR is chosen for subsequent tests thanks to its much lower CTE: $24 \times 10^{-6}$ K$^{-1}$ against $60 \times 10^{-6}$ K$^{-1}$ of the Epotek® T7109-19. The reference thermal conductivity $\kappa_g = 0.85$ W m$^{-1}$ K$^{-1}$ is used in subsequent simulations.

### Mechanical Interface

The surface of the structural components at the interface with the large area silicon sensor must be large (minimum contact point set a 2 mm?) and smooth enough ($Ra$ <1 um?) to avoid punctual stress footprinting introduce to the sensor. At the same time, the glue quantity at

| Glue | $\kappa_g$ datasheet | $\kappa_g$ tests CERN |
|---|---|---|
| Araldite® 2011 | 0.22 | 0.22, 0.23, 0.22 |
| Epoxies® 50-3150 FR | 2.16 | 0.85, 0.83, 0.86 |
| Epotek® T7109-19 | 1.3 | 0.99, 1.01, 1.02 |
| The Polytec TC 423-2 | 3 | — |

**Table 4.3:** Thermal conductivity values of glues given by the official datasheets and CERN tests

the interface must be minimise, where possible. Interface optimisation has been carried out. The baseline procedure consists of two steps. Firstly An. A carbon veil impregnated with glue, which allows a glue control and fine surface finish, is positioned at the carbon foam surface that will be in contact with the silicon sensor The Carbon fleece (veil) used has an area weight of 8 g/m2. It does not have a fixed thickness. The carbon veil is like a sponge. If you press it more, It thinner down. (0.12 mm at @ 10 kPa). We can't measure the thickness of the glue easily and directly. We use shims (0.1mm) to control the glue inserted inside the Carbon Fleece during its impregnation. After that, the impregnated Carbon fleece is attached to the Carbon foam, and a Teflon mould shapes the surface of the Carbon Fleece that will be in contact with the chip later on. At this stage, the mechanical supports have a smooth surface finishing and they are ready for bonding to the Si sensor. The glue is deposited on the top of the shaped Carbon Fleece surface that will touch the chip. The best feedback comes from the CT, where the total thickness of the glue seems to be between 0.2-0.4mm. Still working on it.

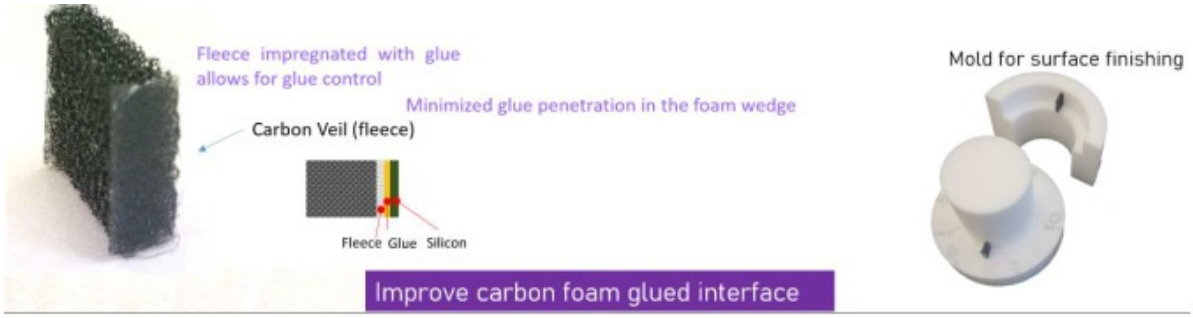


**Figure 4.9:** Gluing procedure of the interface between carbon foam and silicon sensor. new picture. 2 steps +CT scan of the impregnated Carbon foam. .

The thermal resistance of the joint between the carbon foams and the silicon sensors and, in particular, the effect of the amount of glue that penetrates into the foam, is expected to play a major role in the thermal performance of foams. Low values of glue penetration produce thermal resistance, while high values increase the material budget.

To study the mechanical interface, the experimental setup of Fig. 4.6 is used, with samples of the same size as the ones used to measure the pressure loss. Two custom-made polyimide heaters of 100 µm of thickness–consisting of a copper layer of 5 µm surrounded by two polyimide layers ($\kappa = 0.2$ W m$^{-1}$ K$^{-1}$) of 25 and 75 µm—are placed in contact with the foam to represent the heat dissipation of the silicon sensors (see Fig. 4.10a), and the temperatures of the sides of the heater that are not in contact with the foam are measured by two PT1000 in each heater (see Fig. 4.10b). The PT1000 have planar dimensions of $1.6 \times 1.2$ mm, and are placed in the middle of the flow direction $x$.

The setup aims to represent the thermal interface between the K9 foam and the silicon layers of the ITS3. Previous tests performed at CERN have showed that a direct contact between the foam and the silicon sensor of 50 µm of thickness creates footprints in the sensor, which

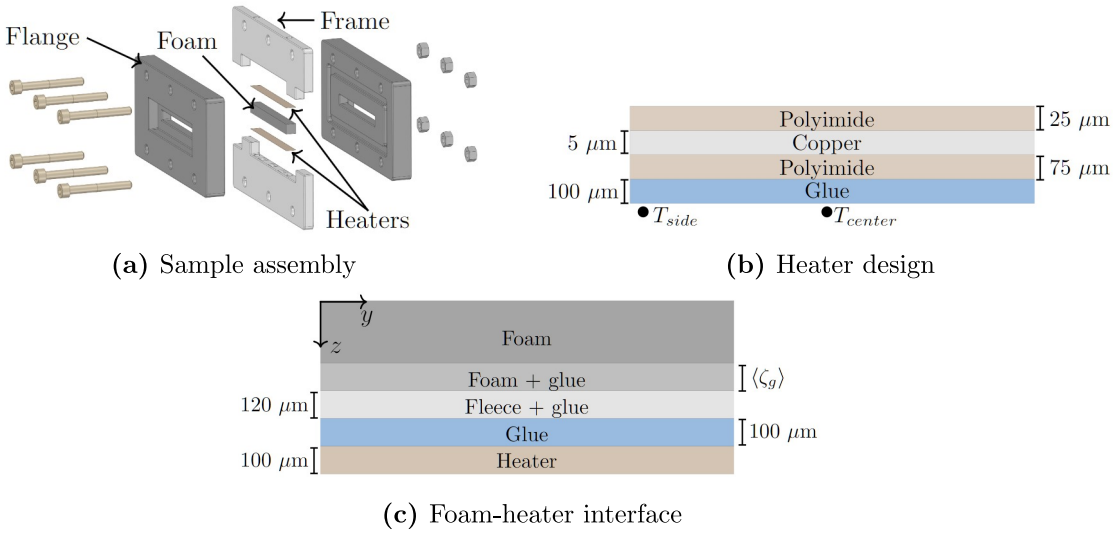


**(a)** Sample assembly **(b)** Heater design

**(c)** Foam-heater interface

**Figure 4.10:** Details of the samples used for the determination of the thermal resistance between the foam and the silicon sensor

constitute a risk of deterioration of the quality of the measurements. To solve that issue, a carbon fleece of 120 µm of thickness and areal density of 8 $\mathrm{g\,m^{-2}}$ is added between the foam and the heater. The fleece glued to the foam provides a smoother contact, with additional contact points that lead to the reduction of the contact resistance and the increase of the shear strength of the joint. Moreover, the presence of the fleece helps the control of the thickness of the glue layer of mean thickness $\langle\zeta_g\rangle$ that penetrates into the foam (see Fig. 4.10c). In the assembly, first the foam is glued to the fleece, and after the curing process the resulting part is glued to the heater. The thickness of the glue layer between the fleece and the heater is 100 µm. As previously mentioned, the glue used is the Epoxies® 50-3150 FR.

To understand the effect of the glue penetration, six samples of mean glue penetration $\langle\zeta_g\rangle = 30, 80, 130, 180, 280$ and 380 µm are tested in the setup. Based on Fig. 4.10c, in the simulations the foam-heater interface is modeled as a layer of $100 + 120 + \langle\zeta_g\rangle$ of thickness, with the thermal conductivity equal to the glue thermal conductivity. Taking as a reference the experimental data obtained by the CMS Collaboration, the optimum penetration of $\langle\zeta_g\rangle = 250$ µm is considered in the numerical model, thus giving a total glue layer thickness of $100 + 120 + 250 = 470$ µm in the simulations. The heat fluxes of the two heaters are the same and equal to 2000 mW/(m·K), and Since the pressure loss that the fan can provide is limited, seven equispaced holes of 1.5 mm are drilled in the foam that provide a 20 % of reduction in the pressure loss.

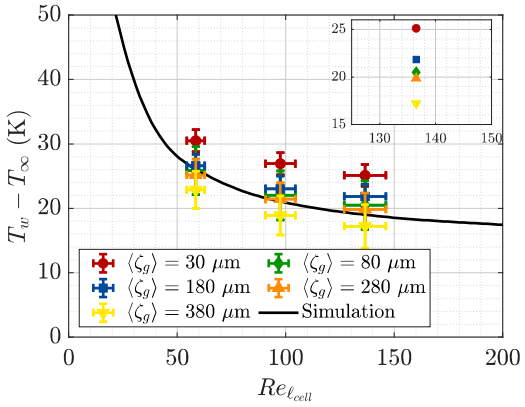


**Figure 4.11:** Influence of the glue penetration on the heater temperature

Fig. 4.11 shows the difference between the heater wall temperature and the freestream temperature for different velocity values. The wall temperature values ($T_w$) are the ones of the temperature sensors located at the center of the heater $T_{center}$ (see Fig. 4.10b). The values of $T_{side}$ are in all cases around 20 % lower than $T_{center}$. This is because the total surface area of the heaters is lower than 6×60 mm because of the presence of the soldering points. It can be concluded that the temperature variations are reasonably bounded with the proposed assembly procedure explained in previous paragraphs. The case of $\langle \zeta_g \rangle = 30$ µm gives the highest temperature values, and is expected to be sensitive to variations in the glue thickness, therefore it is discarded for future tests. The decrease of the heater wall temperature when the glue penetration is increased is explained by the combined effect of two aspects: the decrease of the thermal resistance, and the increase of the thermal conductivity of the foam, since the glue fills the cells of the foam. As a compromise solution, $\langle \zeta_g \rangle = 250$ µm is taken as a reference for the assembly of the ITS3 cooling system.

### 4.3.3 Thermal characterization

#### Experimental setup

An experimental setup has been built at CERN to study the thermal performance of the design explained in Section 4.3.1. Moreover, the assembly procedure—which is not described in this work— is a crucial part of the design, and this setup contributes to the process optimization.

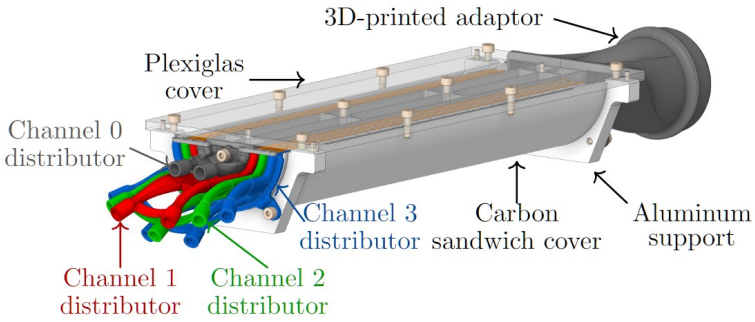


**Figure 4.12:** ITS3 half-barrel used in the experimental setup

Fig. 4.12 shows the core of the setup, which consists of a half-barrel of the design shown in Section 4.3.1 and a carbon sandwich cover (CFRP+thermally-insulating foam+CFRP). The flow distribution system consist of four separated channels.

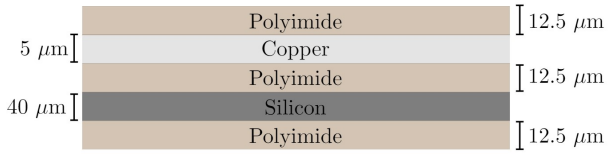


**Figure 4.13:** Layout of the integrated heaters

The heat dissipated by the silicon sensors is modeled with integrated heaters that consist of a silicon wafer of 40 µm, a copper heater of 5 µm, and polyimide layers in between these parts (see Fig. 4.13). The layers are joined with an epoxy glue. The total thickness of the heaters measured is 160-170 µm, and the exact thickness of each of the glue layers is unknown. Since the thermal conductivity of epoxy glues is the same as the polyimide ($\kappa = 0.2$ W m$^{-1}$ K$^{-1}$), the glue layers are considered as an additional thickness of 27.5 µm of the polyimide layers. Thus, the equivalent system consists of the layers of Fig. 4.13 with a thickness of 40 µm of the polyimide layers and a total thickness of $40 \times 4 + 5$ =165 µm. Each layer contains two heaters

to model the power dissipation in the endcap and in the matrix separately (see Fig. 4.14). The layout of the foam-integrated heater interface is the same as the one explained in Fig. 4.10c, but replacing the silicon by the integrated heaters. In all integrated heaters, the temperature of the polyimide layer in contact with the silicon is measured with eight PT1000 temperature sensors of error ±0.15 K. These sensors are joined to the polyimide layers using the same glue used in the foam-heater interface (see Fig. 4.14). The sensors 1 to 4 are placed in contact with the foam.

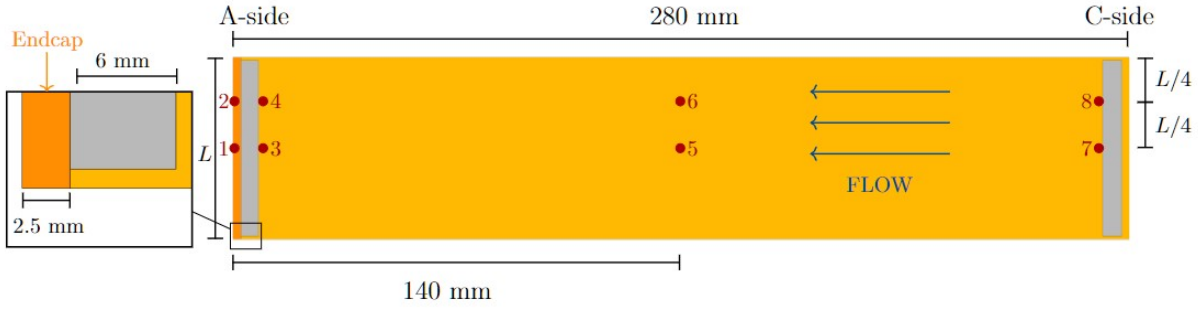


**Figure 4.14:** Location of the temperature sensors in each layer

The air flow is supplied to the system is generated by a fan that can provide a up to $2 \times 10^4$ Pa for a freestream velocity of 20 m/s. The fan includes a frequency inverter so that the operating point can be set manually or with a computer. All of the channels are equipped with an aluminum valve and a mass flow meter. The valves have been designed and produced at CERN to minimize the pressure loss in that area. Due to space limitations related to the installation of the ITS3 in the ALICE cavern, the fan must be placed close to the A-side. Thus, the fan operates such that the flow direction is from the C-side to the A-side; that is, the air expands when passing through the system. This decision is justified because, in the opposite operating condition–where the fan blows air—the inlet temperature is higher than the room temperature due to non-isentropic expansions that are produced by the fan, which are not desirable.

The inlet of the system is a pipe of 50 mm of inner diameter that contains a grid to uniformize the flow and reduce the turbulence levels. The inlet temperature is measured by a temperature sensor, and a velocity sensor is placed to verify that there are no leaks in the system and that the values given by the mass flow meters are correct. The temperature at the outlet of the system is measured by a PT1000 temperature sensor of the same model of the ones used in the heaters.

#### Wind tunnel test thermal validation

#### Comparison between CFD simulations and experiments

Figs. 4.15a, 4.15c and 4.15e depict the temperature in the endcap region measured in the experiments and the one predicted by the numerical model developed in this work. Both methods agree well in the velocity ranges considered, and the simulations overpredict the values slightly in all cases. This is attributed to the thermal resistance produced by the glue between the polyimide layer and the temperature sensors, which is estimated to be around 100 - 200 µm. While the experimental values of $T_3$ and $T_4$ are practically the same in all layers, there is a difference between $T_1$ and $T_2$, specially in Layers 0 and 2. Apart from the differences derived from the contact between the sensor and the layer, it should be noted that in the endcap region the temperature is not uniform, so that a small difference in the location of the sensor can produce differences as the ones shown here.

Fig. 4.16 shows the contours of the temperature variations for two cases of the freestream velocity.

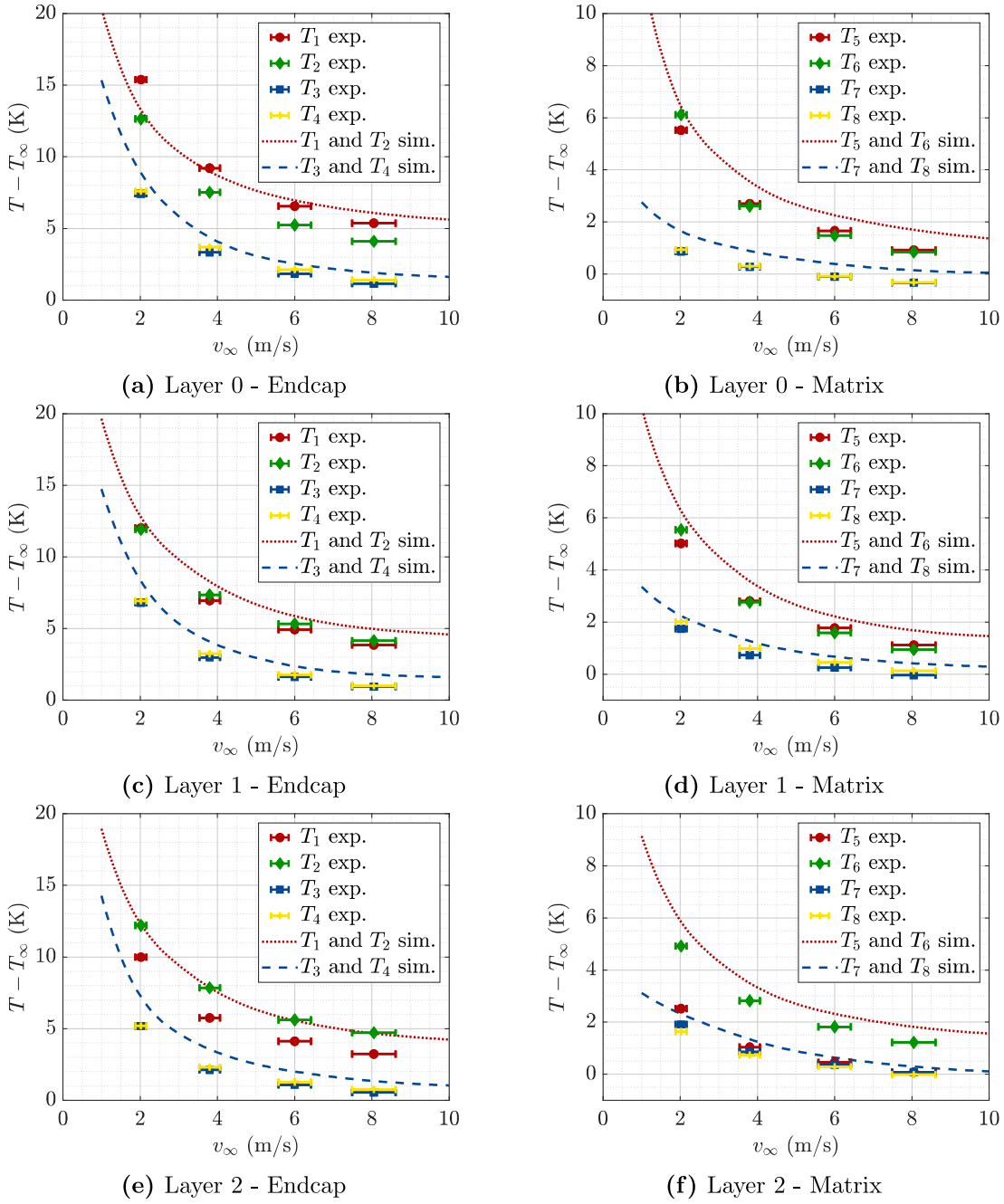


(a) Layer 0 - Endcap

(b) Layer 0 - Matrix

(c) Layer 1 - Endcap

(d) Layer 1 - Matrix

(e) Layer 2 - Endcap

(f) Layer 2 - Matrix

**Figure 4.15:** Temperature variation in the polyimide layers in contact with the silicon layers

### 4.3.4 Mechanical characterisation

#### Aeroelastic analysis and test

on going Impact of airflow on sensor stability, vibration

#### Comparison between CFD and tests

on going

#### Thermoelastic analysis and test

Impact of thermal on sensor stability, thermoelastic movement on going

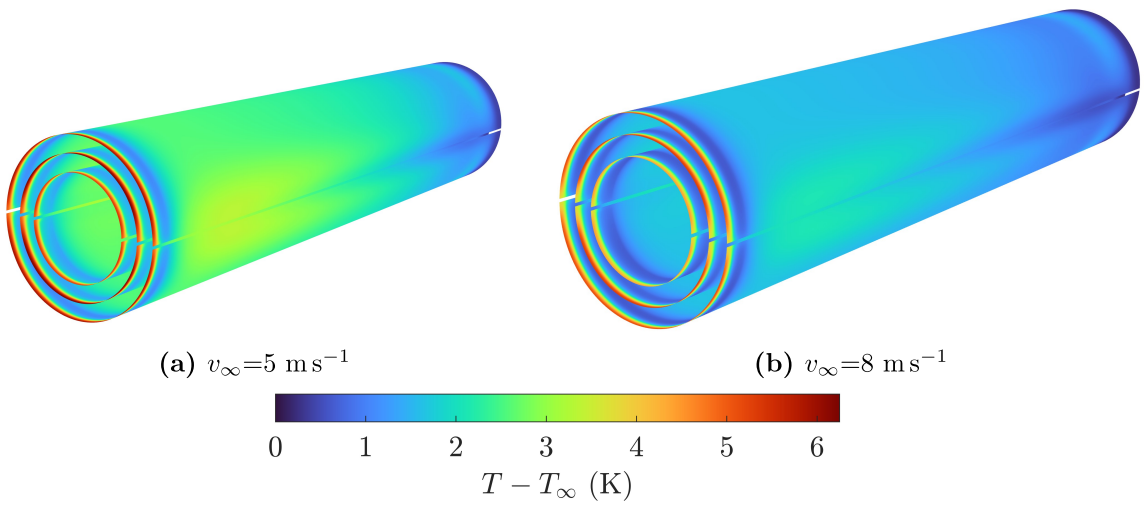


**Figure 4.16:** Contours of the temperature variation in the ITS3 layers

### 4.3.5 Mechanics and cooling alternative designs

#### Mechanics

In parallel to the current baseline mechanical support design based on carbon foam which transfers the load to the CSS, alternative solutions have been investigated with the idea of making each H-layer a self-supported module, not connected to all other H-layers, which can be fully tested. This last aspect can be a further requirement if the yield related to the holding, bending, interconnection and assembly of the silicon h-layer does not allow the H-detector in a monoblock element. For making each layer a self-supported module, the mechanical support of each layer must guarantee a minimum sensor displacement (set to 0.2 mm) along Z and in the circumference direction with respect to the nominal cylindrical layer shape, which requires stiffer support structures. In addition, using carbon foam in an "open" construction poses a risk of loose particles in combination with bare detector surfaces. For these reasons, taking inspiration from the support structure of the previous ITS detectors, two variants based both on lightweight CFRP materials were developed:

- CFRP cradle structure
- CFRP space frame structure

The CFRP cradle structure is formed by the low-mass CF longerons (length ∼287 mm, <2 g weight), rigidly fixed by the relevant CF half-rings visible in Figure 4.17. Composite CF V-shape longerons were produced using high-modulus TORAYCA M55J carbon fiber. They were tested under the center load and found currently to be the most suitable for future applications. Results for TORAYCA M55J show good values of rigidity, suitable for the expected distributed load of bent Si sensors. Results of bending tests of TORAYCA M55J carbon fibre composite V-shape longerons under different centre loads showed linear sagging vs. load at the level of ∼0.35 $\mu$m/g. Results could be further improved by using high-performance carbon fibre like (THORNEL X1100 or TORAYCA® T1100G).

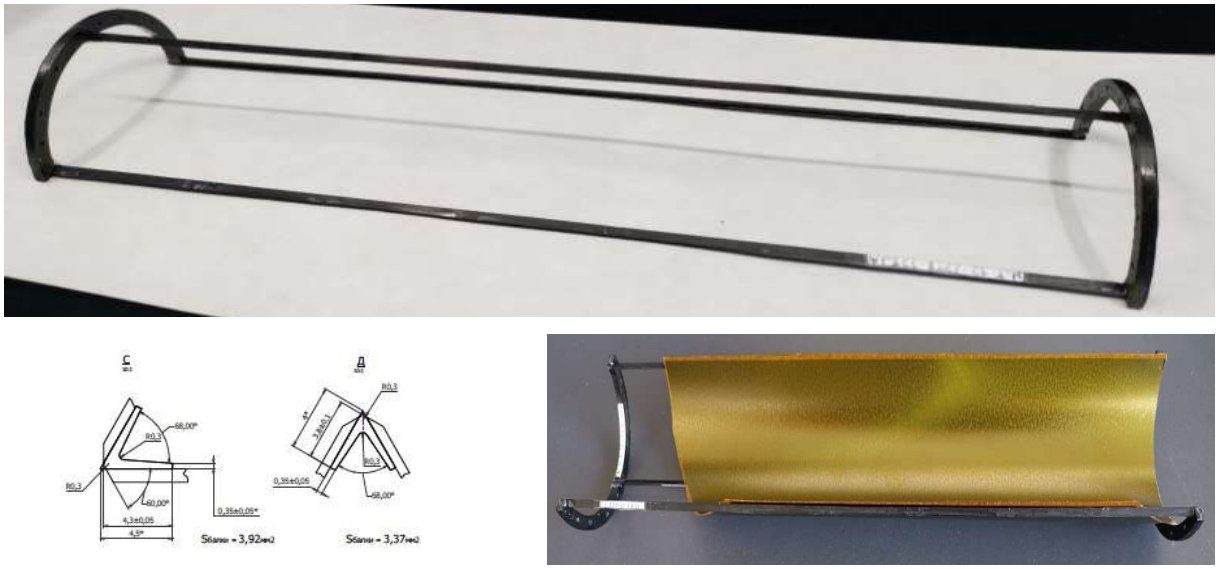

**Figure 4.17:** CFRP cradle structure

The CFRP space frame solution for both half rings and longerons is visible in Figure 4.18. Similar to the space frame used in the ITS2. info about production? The production of longerons and rings is well understood and a self-supported H-layer 2 was built (Figure xxx) using 1 gram total weight of carbon and glue (excluding cooling and support it provides ) this is approximately 30% of the 3.3grams silicon sheet.

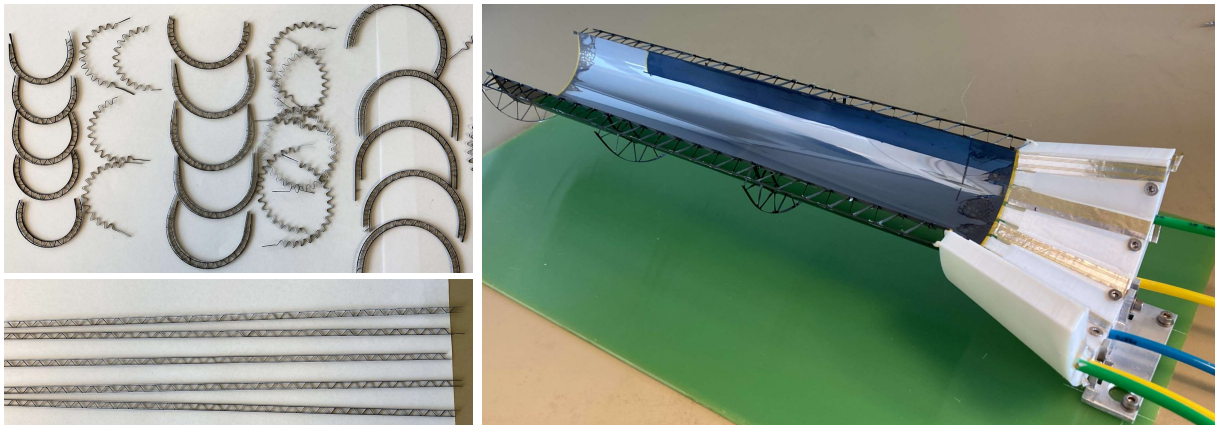

**Figure 4.18:** CFRP space frame structure

The space frame alternative would grant approx. 50 % weight reduction with respect to the carbon foam one and, therefore, a considerable gain on the material budget (Table xxx).

However, the requirement in the sensor positioning, together with the self-supported layer concept, requires to implementation of additional half rings at the sensitive region (Figure XXX) to stiffness the assembly, which penalised the overall material budget contribution. Thermoelastic stress and displacement induced by the different materials (Silicon sensors, glue, carbon foam radiators and CFRP structural supports) imply a detailed analysis to guarantee sensor integrity and stability. A demonstration of a full L0-L1-L2 with re-mountable layers and some degrees of freedom to allow for different thermal expansions is also under construction.

Both solutions are promising candidates for the final choice. Even if the self-support concept will not be adopted, the two alternatives could be implemented in the proposed baseline design where the H-detector is the minimum replaceable component.

### Cooling

The thermal management of the entire H-detector is strongly dependent on the sensor design development. Even if the cooling strategies based on airflow as a refrigerant and thermal conductive carbon foam radiator as thermal efficient improvement at the end-cap sensor region showed a sufficient cooling performance for current projections on final power, well understood by simulations and measurements, alternative design strategies have been exploited.

A preliminary screening of different materials for producing H-ring radiators was done. The main results are visible in Figure 4.19.

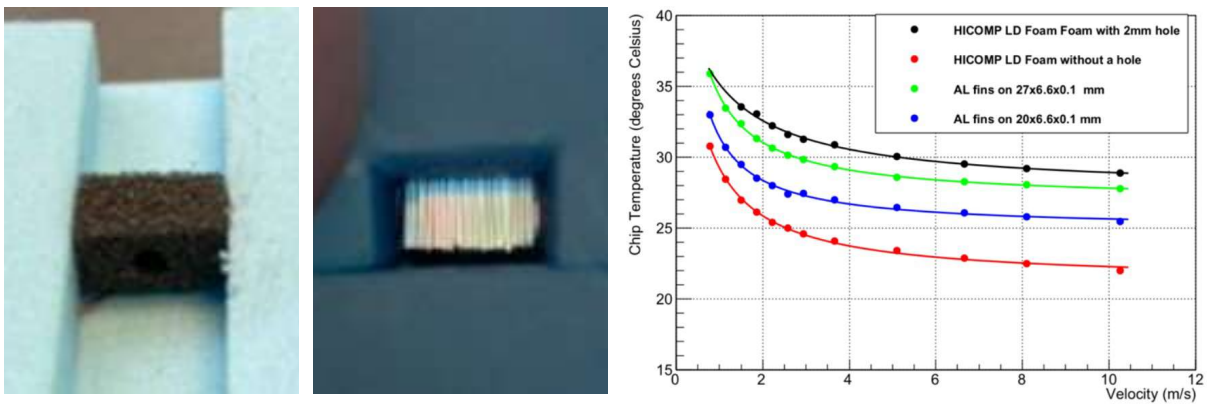


**Figure 4.19:** Single block H-ring radiator

Small-scale samples of “carbon foam” coolers with and without holes and several glueing methods to get a better understanding of cooling on this scale were produced, tested and compared with aluminium and carbon fin structures (Figure 4.19.b). The results highlighted that the carbon foam cooling structures work best without holes at the cost of a high-pressure drop. Fin structures have lower cooling performances and prove to be extremely difficult to build on a sufficiently small scale in a non-metal (e.g. carbon).

Based on the above campaign, two proposed alternatives to the baseline radiator design have been developed:

- Single block H-ring radiator
- H-ring with integrated water cooling line

The carbon foam H-ring radiator and its cooling ducts can be embedded in a single component (Figure 4.20), forming a single block H-ring radiator. In this way, the entire gas mass flow is able to pass into the carbon foam radiator.

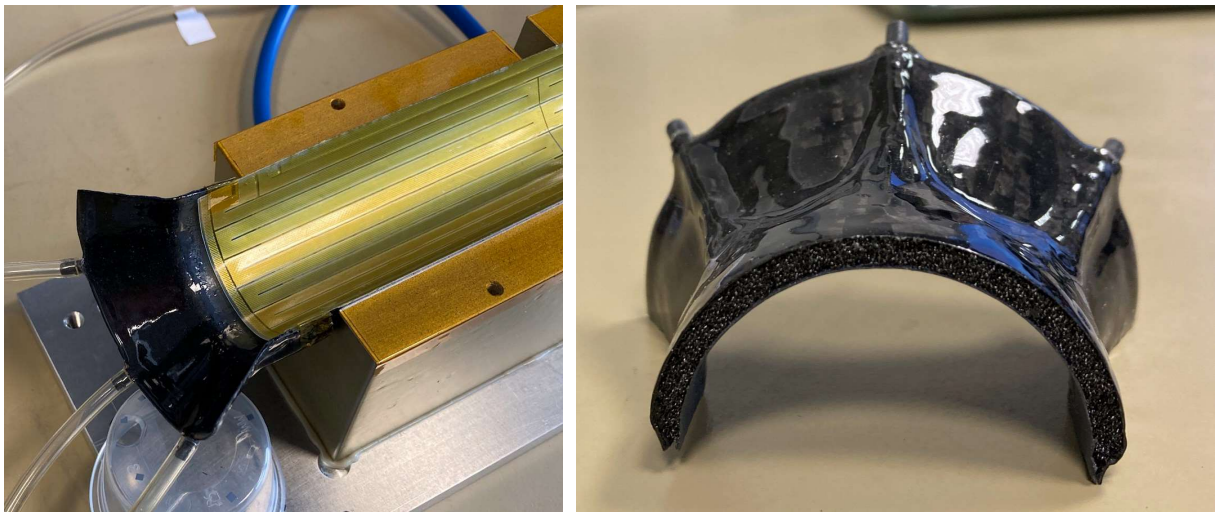

**Figure 4.20:** Single block H-ring radiator

A dummy H-layer 0 was implemented with the single block solution without carbon foam holes (Figure 4.20.a and .b), and a confined carbon air distribution is demonstrated with a thermal resistance of 4 K/W at approximately 4m/s airspeed at the exit of the dummy detector.

The main aspect to be investigated for the single block alternative is the encumbrance problem, as the same area at the interface with the A-side sensor side is shared with the wire-bonding electrical interconnection. Design adjustment and assembly procedure adaptation should be a natural development of this alternative line.

An H-ring with an integrated water cooling line would be an alternative solution for the heat drain coming from higher surface power density (up to 2.2 W/cm$^2$) at the end-cup region. Liquid cooling tubes can be embedded into Pyrolytic Graphite elements (Figure 4.21). The under-pressurized ( 0,9 bar) liquid (water). At the same time, gaps between the Pyrolytic Graphite elements will provide the gas flow access to the matrix sensor region, cooled by either natural or forced convention.

In virtue of possible important vibrations that are inevitably induced from the air flow speed (2-8 m/s) needed to cool the matrix region of the H-layer, a possible alternative based on low-speed (¡0.001 m/s) nitrogen gas cooling was developed (Figure 4.22). A detector mock-up barrel up barrel containing a space blanket outer thermal shell (Figure 4.22.a) housing three cylinder dummy thin sensor layers with embedded heaters was produced. Results of the cold N2 gas (10oC) cooling tests for the thermal mock-up of L2 cylinder layer are shown in Figure 4.22.b.

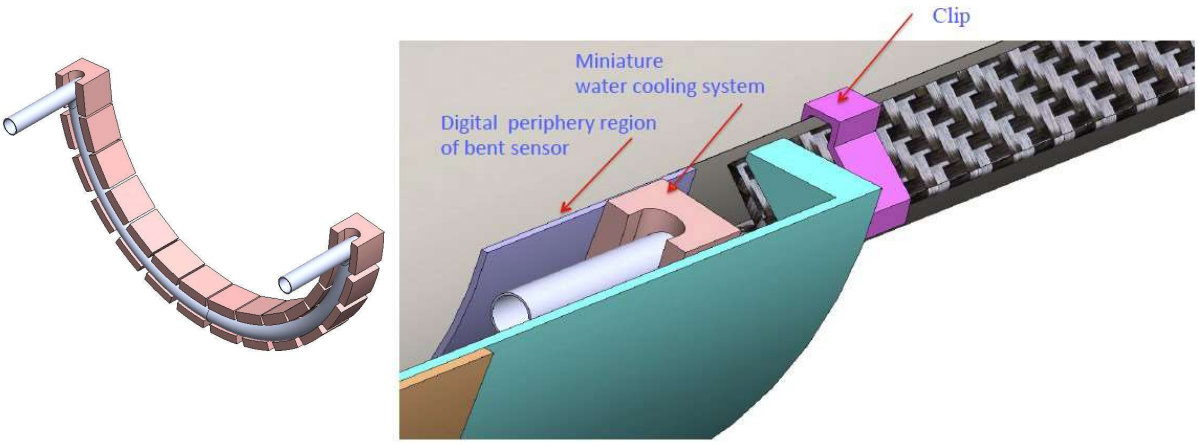


**Figure 4.21:** H-ring with integrated water cooling line

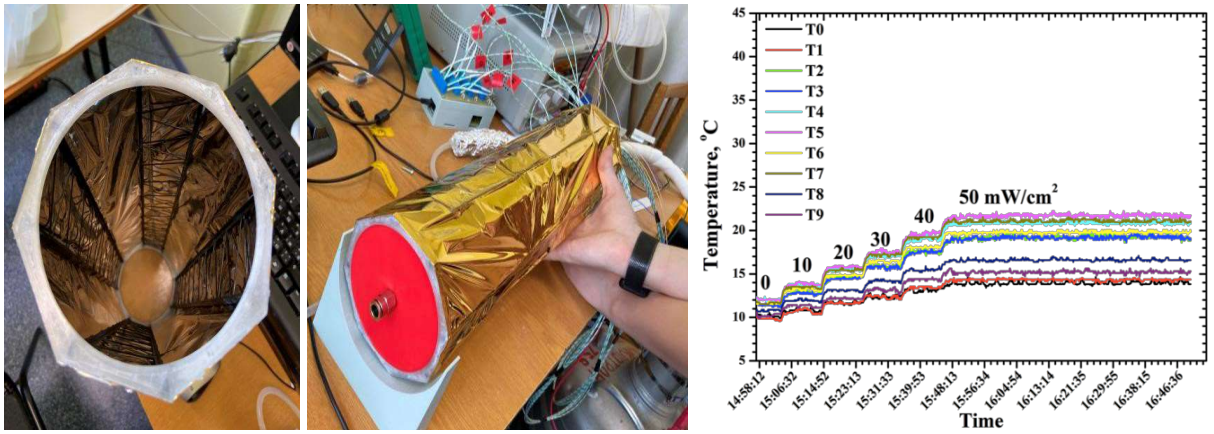


**Figure 4.22:** Nitrogen gas cooling option. (a) photo of the detector mock-up barrel and (b) temperature distribution along the thermal mock-up cylinder layer 2 under different heat loads (the inlet temperature of the cold N2 was 10oC). The space blanket self-supported outer thermal shell and the mock-up of 3 silicon cylinder layers inside the thermal space blanket's outer shell were equipped with 10 thermocouples (T0,T1...T9). 9 of them are mounted on top of the cylinder layers of dummy sensors, while one is placed inside on the dummy beam-pipe.

The cold gas cooling (nitrogen) has demonstrated its feasibility in providing the heat drain at the level of up to 50 mW/cm2 with very low speed of flow. Separate flow distribution of cold N2 between layers L0 L1 and L2, as well as between the beam-pipe and L0 and between layer L2 and the thermal outer space blanket shell, is foreseen with the account of relevant mean heat power dissipation. Work is in progress.

## 4.4 Flexible printed circuit

Antoine part The FPC is six layers printed circuit manufactured as three double sides FPC tails, called Top, Mid and Bot. The there FPC tails are stacked and manually assembled together forming the final FPC, which serves a single H-layer. This configuration helps the passive components assembly, sited on FPC tail. In addition, the FPC is divided into sections, each corresponding to a section of the sensor, respectively 3,4 and 5, related to the detector layers L0, L1 and L2. Fig. 1.

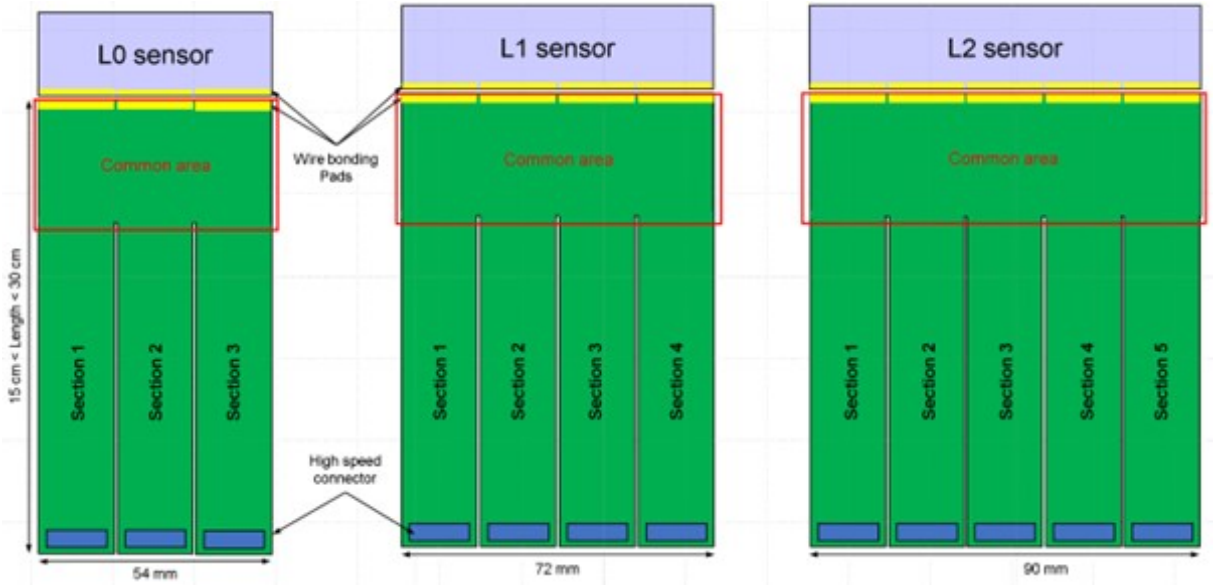


**Figure 4.23:** Schematic view of the three FPCs for the three H-layers. (a), (b) and (c).

The Mid and Bot FPC have 25 µm thick polyimide as substrate and two conducting layers of cooper each, 35 µm thick. The Top FPC has 75 µm thick polyimide as substrate and two conducting layers of cooper, 35 µm thick.

Each section of the FPC provides independently analogue power and bias voltage, digital core and digital IO power, digital lines carrying signal at 2.5 Gbit/s and 3 differential buses for slow control clock at 40 MHz. Fig. 2. All the signal lines stand on the top layer, without signal transition via to optimize the signal integrity.

The connection between the FPC and the pixel chips are made via ultrasonic wire bonding. Power supply and I/O pads are concentrated along the edge of the common area of the FPC. Fig. 3, 4 & 5.

### 4.4.1 FPC tails assembly

First, the three double side FPC are populated with passive components, decoupling capacitors, and connectors, except for the Top FPC where only the connectors are assembled. Secondly, the tree FPC tails are assembled together with the help of a dedicated tool (Figure xxx).

To avoid any stress on the connection between the FPCs and decoupling capacitors in the common area. The assembly of the three FPCs tails is made as the final assembly shape in a cylindrical manner.

To assemble the three different detector layers, L0, L1 and L2 three different tools diameter are necessary. The tool is a mandrel with the corresponding detector layer diameter held by 2 foots. The mandrel can rotate to help the soldering process under microscope.

The FPC Bot is fixed on the mandrel, and the connection areas are tined. Next, the FPC Mid is stacked and fixed over. The two FPCs are soldered together with their own connection areas.

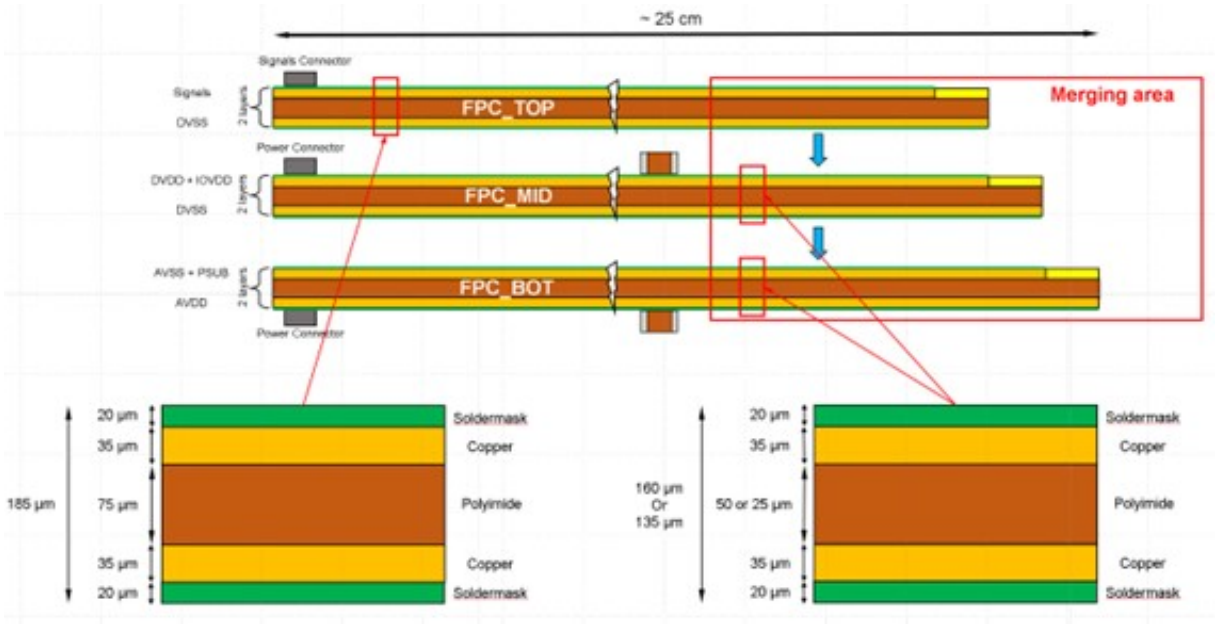


**Figure 4.24:** FPC layer stack-up. (a), (b) and (c).

The other connection areas are also tined. The FPC Top is then stacked over and soldered. The final step is soldering decoupling capacitors in the common area.

### 4.4.2 FPC electrical characterization

TO BE DONE

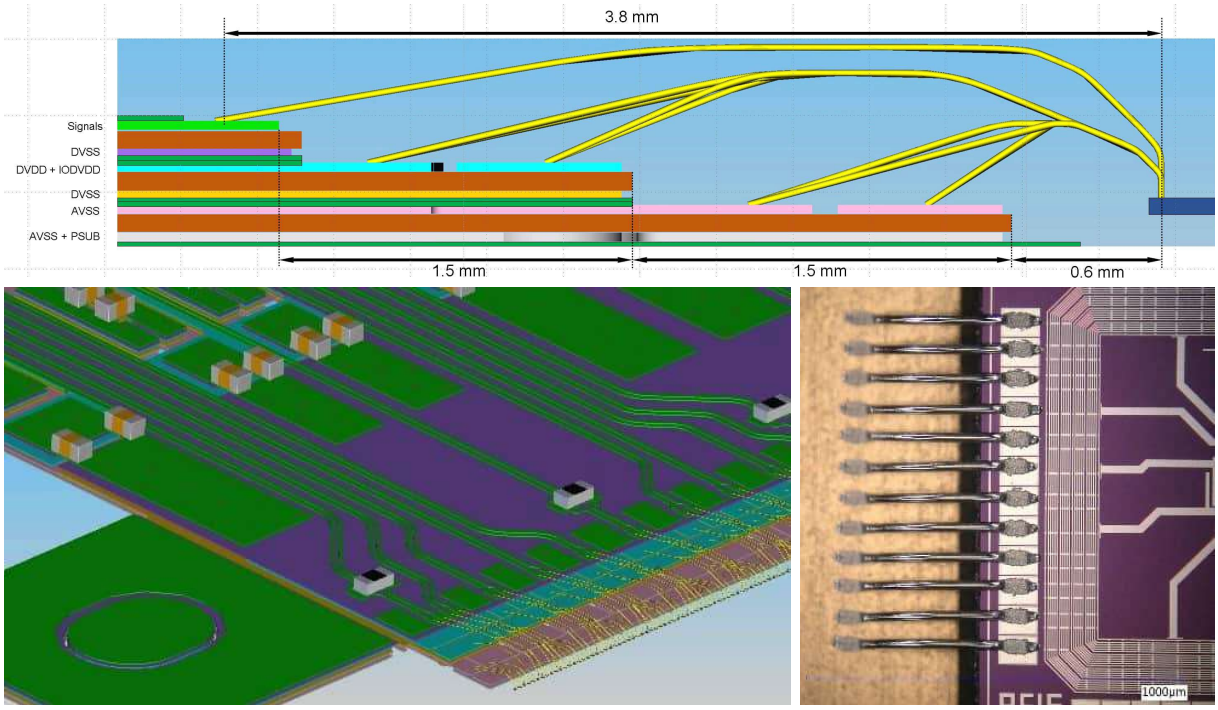


**Figure 4.25:** Details of the Wire-bonded interconnection. (a) Side view of the FPC, sensor and wire bonds, (b) 3D view of a wire bonded FPC section and (c) photography of wire-bonding between FPC and dummy sensor.

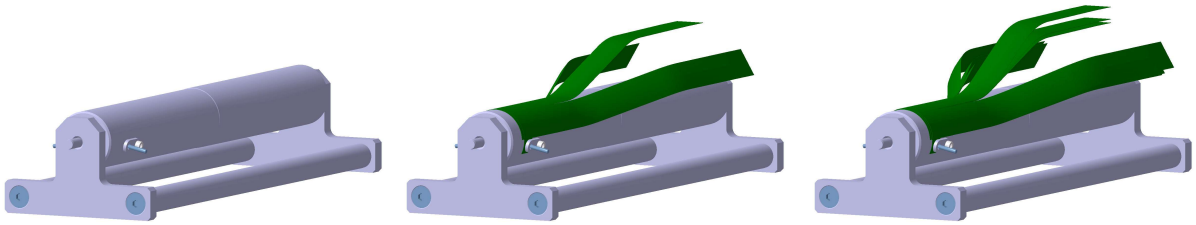

**Figure 4.26:** FPC assembly of layer L0

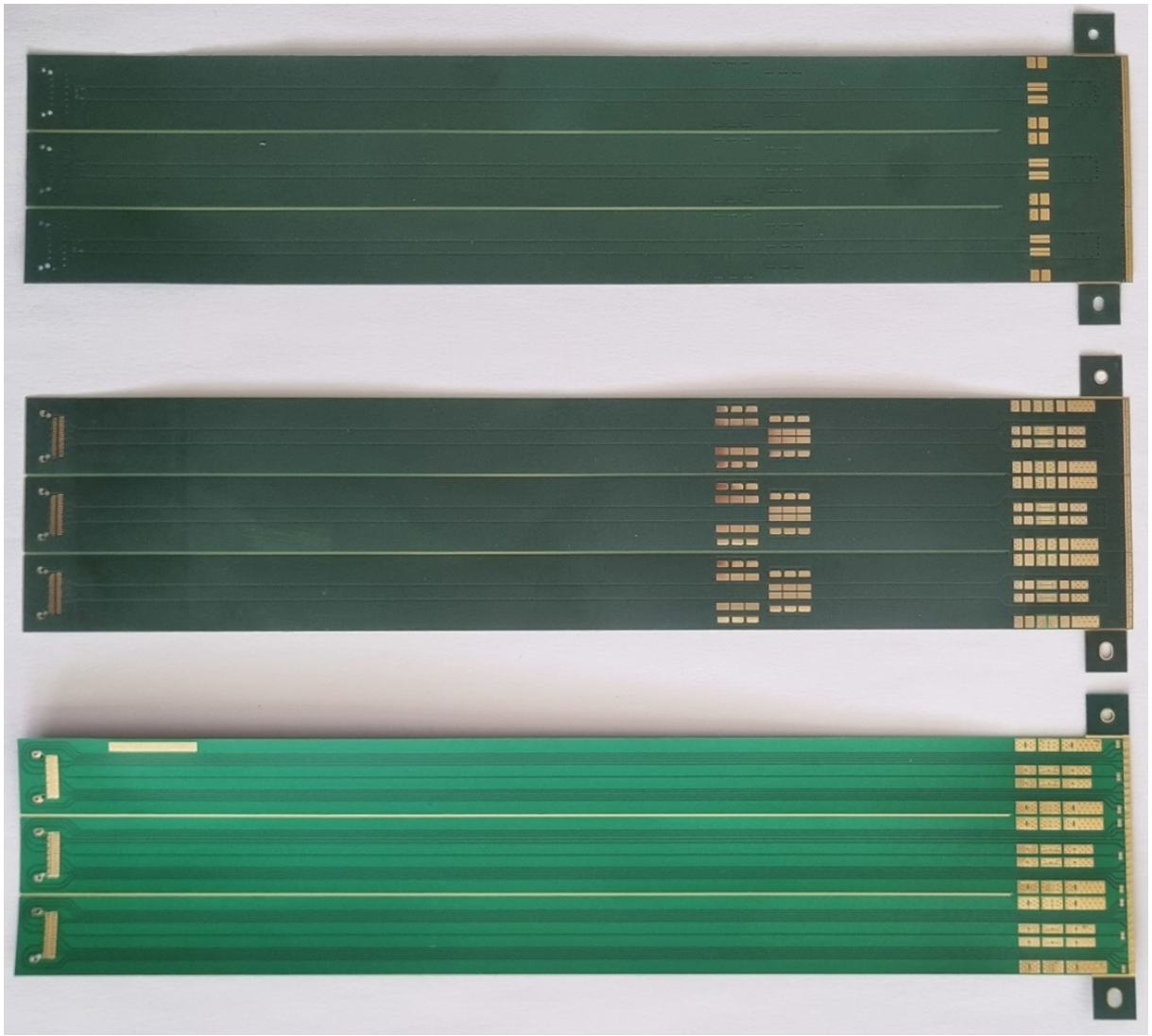

**Figure 4.27:** L0 FPC, Bot, Mid and Top Layer respectively

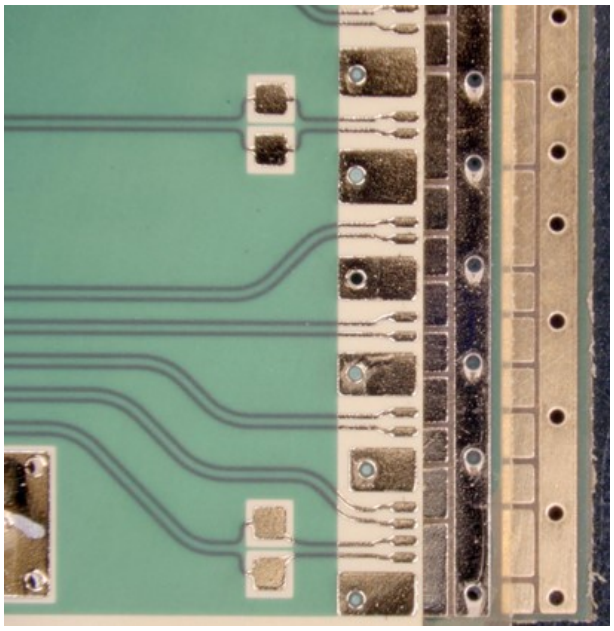

**Figure 4.28:** Detail of the bonding area layer L0 FPC

## 4.5 Detector assembly

The H-detector assembly procedure is composed of two main sub-assembly sequences:

- **H-layer assembly:** Each H-layer follows a similar assembly procedure (Sec.4.5.1).
- **H-layers integration:** The H-layers are integrated, forming the H-detector (Sec.4.5.3).

In order to minimise particle contamination and possible sensor and assembly failures, the entire assembly is supposed to be done in a controlled clean room environment (CERN DFS laboratory), the sensor handling minimised, and the assembly performed under a single jig denoted as Multi Purpose Jig (MPJ) and visible in Figure 4.29).

**Figure 4.29:** Multi Purpose Jig. new picture.

During sub-assembly sequences, several mechanical and electrical inspections and metrology steps are foreseen. Metrology of the latest H-detector prototype, based on X-ray computed tomography scan, is in Sec.4.5.4.

### 4.5.1 H-layer assembly

The H-layer assembly is divided into three steps here below described and visible in Figure 4.30.

- **H-layer bending:** Each H-layer is bent on a dedicated Mandrel, which provide the correct cylindrical shape.
- **H-layer electrical interconnection to the FPC:** The FPC is aligned with the Si sensor. Wire-bonding is selected as the baseline electrical interconnection between large-area sensors and FPC.
- **H-layer bonding to mechanics:** The mechanical supports are then glued with accurate jigs.

a

a

a

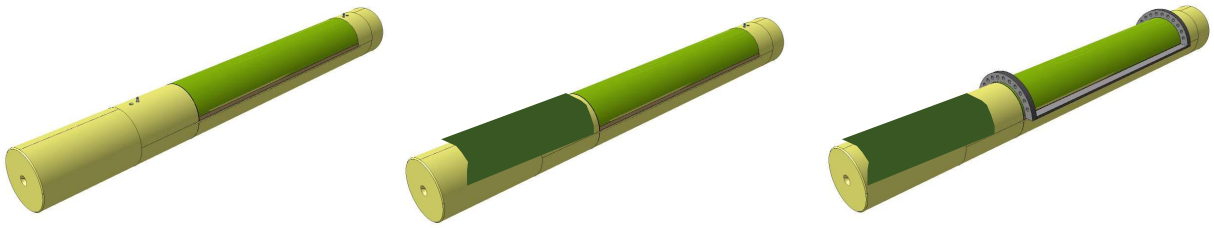

**Figure 4.30:** H-layer sub-assembly sequence. TO BE DONE. Overview of the sequence. .

### H-layer bending

The bending procedure of a large-area silicon sensor follows the steps described in Figure 4.31 and Figure 4.32. Manual alignment under a digital microscope. The flat sensor is positioned and aligned onto the mandrel. An adhesive polyimide tape holds the Si sensor to the mandrel. In the following step, a mylar foil is used to bend the H-layer while the mandrel assures its cylindricity. A second polyimide foil, placed on the other long edge extremity of the sensor, is stacked in contact with the mandrel, guaranteeing sensor holding. Finally, the mylar foil is removed and the sensor remained tight to the mandrel.

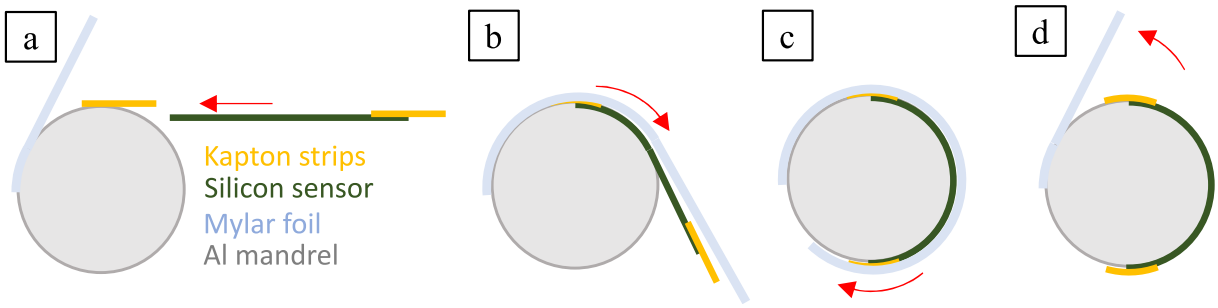


**Figure 4.31:** Bending procedure of a large-area silicon sensor. (a) , (b), (c) and (d)

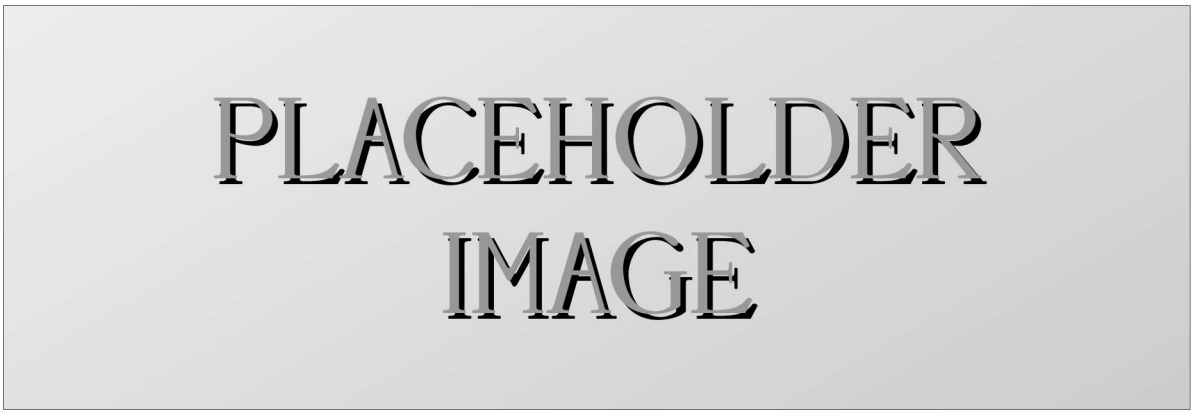


**Figure 4.32:** Bending of a naked silicon H-layer prototype

#### Layer to FPC connection

During this step, the FPC is placed and correctly aligned onto the mandrel with respect to the H-layer sensor. The MPJ is then positioned under the wire-bonding machine for electrical interconnection (Figure 4.33). After that, the H-layer sensor is electrically tested. Comment Domenico - go the description of the inclusion step of the FPC in the detector with reference to the fact that the standard interconnection procedure is wire bonding, but without giving any result or description of the technical characteristics of the bonding

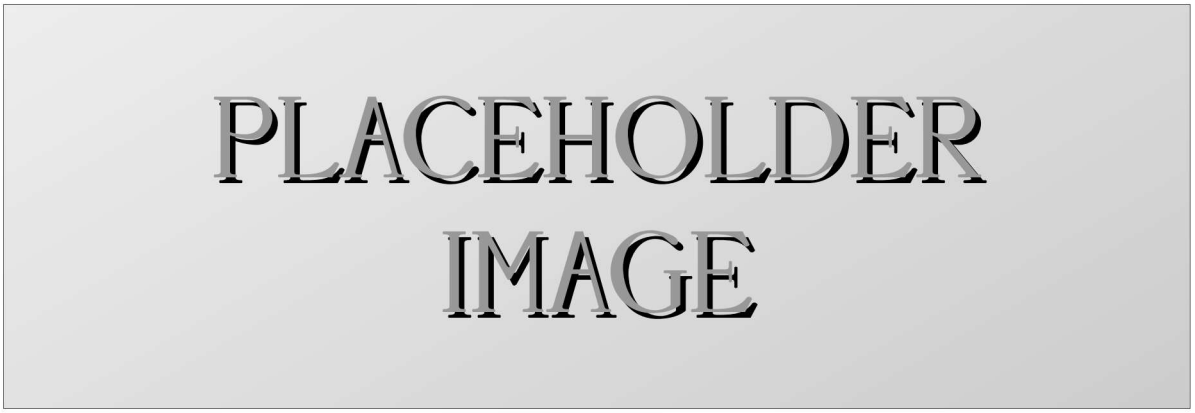


**Figure 4.33:** Wire-bonding step

#### H-layer bonding to mechanics:

Once the electrical connection step is completed, the FPC and the H-layer sensor are ready for the mechanics bonding. Several jigs are used to correctly place the support structures onto the FPC and the H-layer sensor (Figure 4.34). The glueing interface of the carbon support structure was optimised as described in Section 4.3.2.

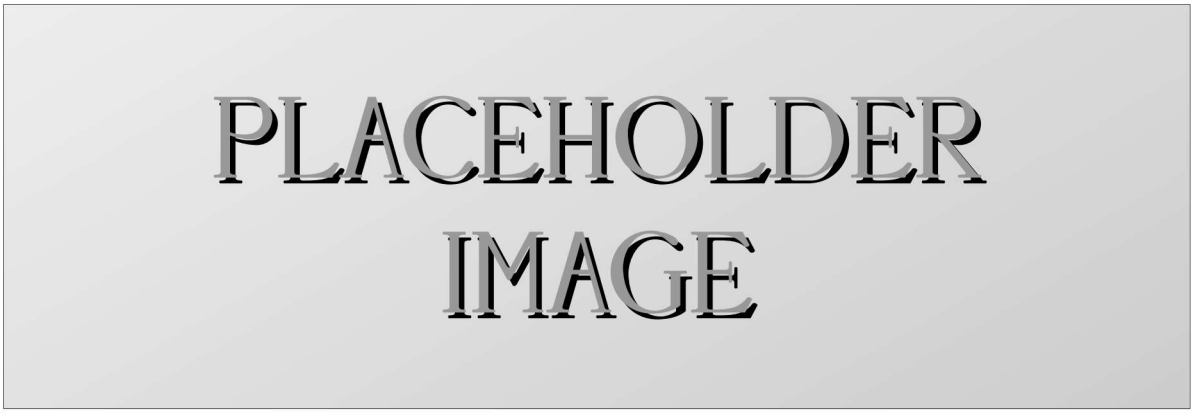


**Figure 4.34:** Bonding of the mechanical support structures

At this stage, the shape is still guaranteed by the mandrel. The bonding to mechanics step can also be done after the electrical interconnection step if required by future constraints with no-critical impact from the mechanical point of view.

### 4.5.2 Layers test and characterisation

Massimo comment: to be done by?

### 4.5.3 H-layers integration

This integration is divided into three main steps described below and visible in Figure xxx:

- **H-L2 bonding to CSS:** The support structure of the H-L2 are glued on the CSS. Alignment is foreseen through reference pins at the mandrel and CSS alignment jig.
- **H-L1 bonding to H-L2+CSS:** Similarly to the previous
- **H-L0 bonding to H-L1+H-L2+CSS**

During each step, an H-layer is disjointed from the mandrel, while the structural support is guaranteed by the CSS. Electrical tests are foreseen to re-verify the proper working of the integrated H-layer sensor.

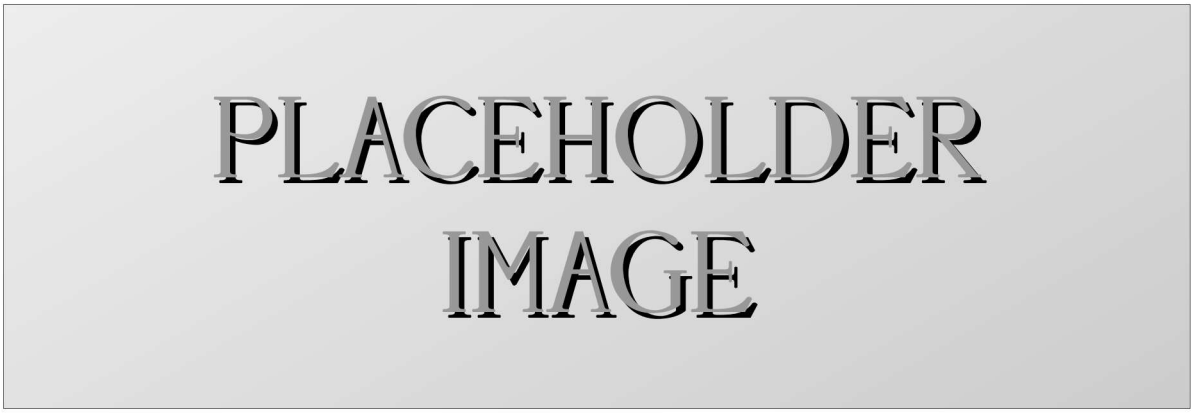


**Figure 4.35:** H-layer integration steps. (a) (b) and (c). new pict.

### 4.5.4 H-detector inspection

Due to the impossible to visually inspect inside the H-detector once assembled, X-ray computed tomography scans are considered as baseline tool to verify H-detector integrity and perform final H-layer metrology. The X-ray scan performed for the latest H-prototype is visible in Figure xxx. 50 um TBD of it is ok.

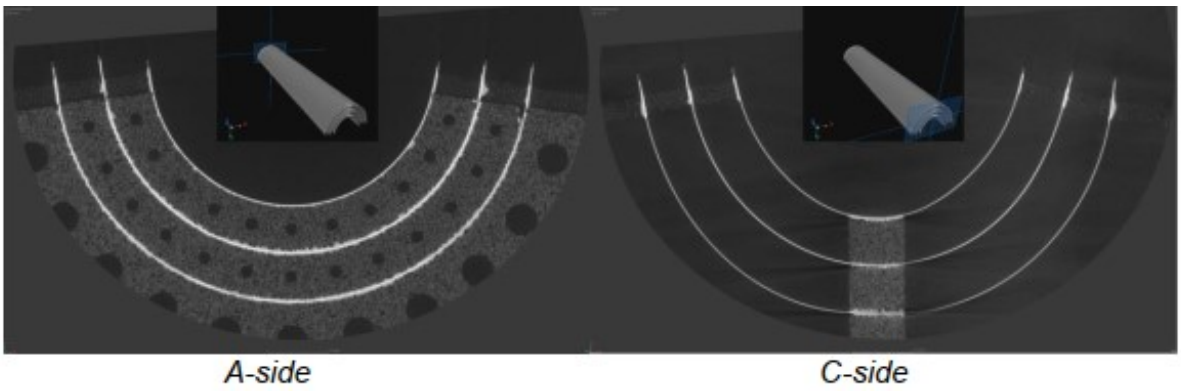


**Figure 4.36:** X-ray computed tomography of BBM2. new picture.. .

### 4.5.5 Detector alternative layout

Alternative layouts are investigated. Implementing an additional detection layer with a radius greater than 50 mm can be a future requirement. Similar mechanics and cooling (carbon foam and air cooling) adopted for the three inner layers can be, in principle, adopted for the additional one (Figure 4.37). Iterative steps, which involve design, analysis, prototype production and test are required to validate the new layout.

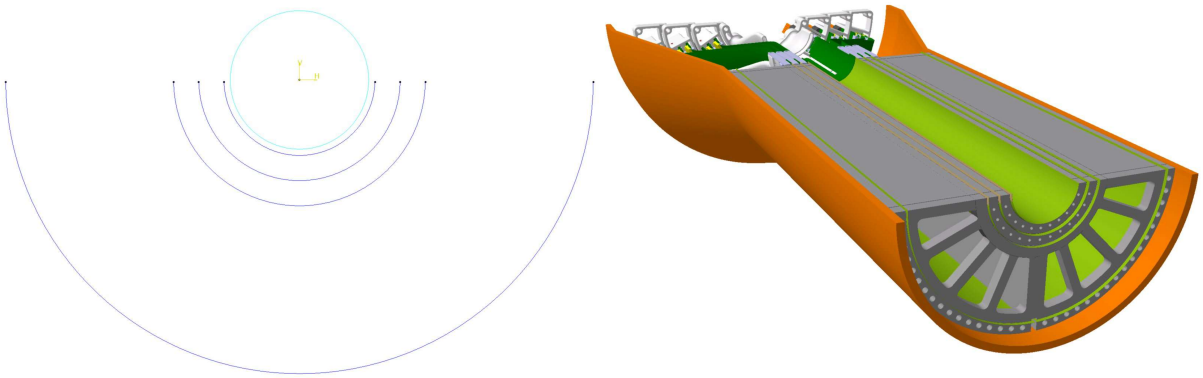

**Figure 4.37:** Additional detection layer. (a) schematic view and (b) CAD model. new pict.

An additional alternative, which depends on the design evolution of the large-area Si sensors, would require supplying a power line to the sensors on the C-side. In this case, an additional FPC or sinple wires will have to be routed from A-side outside the CYSS up to the edge of the layers on the C-side. Similarly, an additional cooling radiator and its cooling duct and routing could be required depending on the estimated surface power density that the sensor dissipates at the C-side endcap region. A tentative design, with services implemented on the C-Side is Visible in Figure 4.38 PUT AS BASELINE OR ALTERNATIVE?.

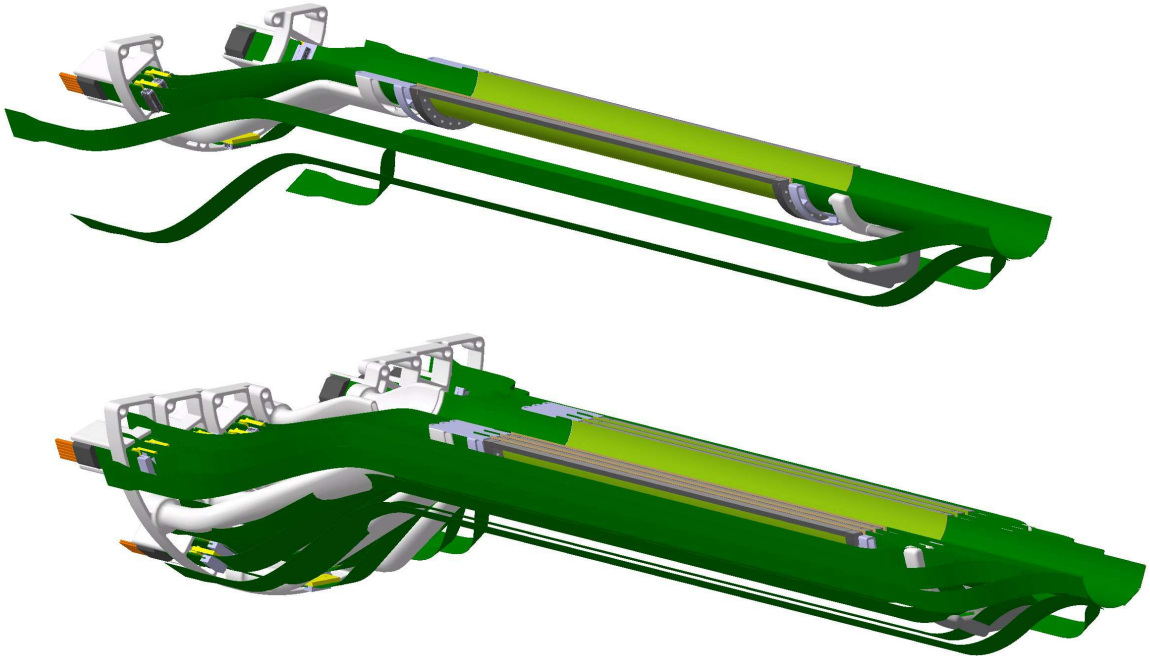

**Figure 4.38:** Services at the C-side.